Article

Not peer-reviewed version

# Investigation of Microstructural Characterization and Tensile Deformation Mechanisms in Inconel 617 Welded Joints Produced by GTAW

Mingyang Zhao , Lang Wang , Wenhao Ren , Yuxin Wang * , Tao Zhang , Zhengzong Chen *

Posted Date: 18 December 2025

doi: 10.20944/preprints202512.1597.v1

Keywords: Inconel 617 alloy; microstructure; tensile properties; deformation mechanisms

 doi:10.20944/preprints202512.1597.v1



*Article*

# Investigation of Microstructural Characterization and Tensile Deformation Mechanisms in Inconel 617 Welded Joints Produced by GTAW

**Mingyang Zhao [1,2,3], Lang Wang [4], Wenhao Ren [1,3], Yuxin Wang [4,*], Tao Zhang [5] and Zhengzong Chen [1,3,*]**

[1] Research Institute of Special Steels, Central Iron and Steel Research Institute Co., Ltd., Beijing 100081, China
[2] School of Materials and Metallurgy，University of Science and Technology Liaoning, Anshan 114051, China
[3] State Key Laboratory of Advanced Special Steel, Beijing 100081, China
[4] Nuclear Equipment Division, China Nuclear Power Engineering Co., Ltd., Beijing 100840, China
[5] Lanzhou LS Heavy Equipment Co., Ltd., Lanzhou 730314, China
* Correspondence: 13720008981@163.com (Y.W.); chenzhengzong@nercast.com (Z.C.)

**Abstract**

The microstructural evolution and tensile behavior of Inconel 617 welded joints produced by gas tungsten arc welding (GTAW) with ERNiCrCoMo-1 filler were systematically investigated. Detailed microstructural characterization revealed that Cr-rich $M_{23}C_6$ and Ti-rich MC carbides are the dominant precipitates, while Mo-rich $M_6C$ forms locally along grain boundaries after thermal exposure. The fusion and weld zones exhibit fine dendritic morphologies with uniformly distributed precipitates, resulting in significant strengthening through precipitation and dislocation-pinning mechanisms. Owing to the low heat input and compositional compatibility between the weld and base metals, the heat-affected zone remains extremely narrow and free of compositional transitions. The welded joint attains tensile strengths of 920 MPa at room temperature and 605.5 MPa at 750 °C, corresponding to joint efficiencies of 117% and 121%, respectively, with fracture consistently occurring in the base metal. Deformation analysis shows that plasticity at room temperature is governed by planar slip and dislocation entanglement, whereas deformation twinning predominates at elevated temperatures owing to the reduced stacking-fault energy and the pinning effect of $M_{23}C_6$ carbides. These results provide key insights into the deformation and strengthening mechanisms controlling the high-temperature performance of GTAW-welded Inconel 617 joints and offer guidance for their application in advanced nuclear and high-temperature energy systems.

**Keywords:** Inconel 617 alloy; microstructure; tensile properties; deformation mechanisms

## 1. Introduction

High-temperature alloys play a vital role in the development of nuclear reactors owing to their exceptional strength, oxidation resistance, corrosion resistance, fatigue resistance, creep resistance, and structural stability [1]. Among them, Inconel 617—a Ni-Cr-Co-Mo alloy—is distinguished by its superior high-temperature strength and heat resistance, making it particularly suitable for structural components in chemical processing equipment, nuclear reactors, and aerospace systems [2–5]. This alloy has been incorporated into the ASME nuclear standards as one of six materials approved for high-temperature nuclear components. Moreover, Inconel 617 is listed in ASME Code Case N-898, which specifies its application in Class A elevated-temperature service under Section III, Division 5,

 doi:10.20944/preprints202512.1597.v1



with a design life of 100,000 hours. Such comprehensive qualification data further underscores its extensive potential for use in advanced nuclear power systems [6].

With the widespread adoption of Inconel 617 alloy, research on its weldability has attracted increasing attention. Welding is inevitably required at multiple stages during the fabrication of heat exchangers and pipelines for high-temperature gas-cooled reactors [7]. Despite the structural complexity of these components, welding remains indispensable in their manufacture. Considering factors such as joint geometry and component dimensions, the gas tungsten arc welding (GTAW) process has been identified as the most suitable technique. Welded joints play a pivotal role in industrial systems, serving as critical connections between components, and their integrity directly influences overall system performance. Nevertheless, welded joints are well known to exhibit a higher susceptibility to failure under high-temperature conditions, primarily due to microstructural and mechanical heterogeneity across different regions of the joint [8,9].

In recent years, extensive research has been carried out worldwide on the engineering applications of Inconel 617 alloy. Reference [10] reported the welding of 22Cr15Ni3.5CuNbN steel using ERNiCrCoMo-1 filler wire, revealing Ti-rich precipitates in the weld metal and Cr- and Nb-rich precipitates in the base metal. The study further demonstrated that grain refinement induced by welding markedly influences the alloy's mechanical properties. References [11–14] examined the mechanical performance and microstructural evolution of dissimilar Inconel 617 welded joints at elevated temperatures. These investigations identified $M_{23}C_6$ (Cr-rich) and MC (Ti-rich) phases as the dominant precipitates in Inconel 617, while the ERNiCrCoMo-1 filler promotes the formation of Mo-rich $M_6C$ phases after thermal exposure, thereby significantly modifying the weld microstructure. Softening of the base-metal matrix, resulting from the welding process or deformation-induced precipitate evolution, can cause instability and premature failure of the joint under high-temperature or cyclic loading conditions. Overall, the high alloying content renders the welding of nickel-based superalloys challenging and susceptible to defects. Consequently, systematic evaluation of welding processes and detailed analyses of weld microstructure and mechanical behavior are essential.

In this study, Inconel 617 alloy was welded using the gas tungsten arc welding (GTAW) technique. The precipitates in different regions of the welded joint were characterized both qualitatively and quantitatively. Tensile tests were performed at room temperature and 750 °C, and the fracture morphology and deformation mechanisms of the joints were subsequently examined. The results provide theoretical insight into the welding performance and practical applicability of Inconel 617 alloy and its welded joints.

## 2. Materials and Methods

### *2.1. Materials and Experimental Procedures*

The Inconel 617 alloy ingot was produced through a dual-melting route comprising vacuum induction melting followed by vacuum arc remelting. After subsequent forging and rolling, alloy plates with a thickness of 23 mm were fabricated. Multi-pass, multi-layer welding of these plates was performed using manual GTAW with imported ERNiCrCoMo-1 filler wire (Φ2.4 mm). The welding parameters were as follows: heat input, 0.78 kJ $mm^{-1}$; current, 110–125 A; voltage, 9–13 V; and travel speed, 125–160 mm $min^{-1}$. The welded plates are shown in Figure 1(a). A V-groove configuration with a groove angle of 60° was adopted for the joint, as illustrated in Figure 1(b). Post-weld non-destructive testing was conducted in accordance with ASME BPVC Section V and HBB-5000 standards. Plates that passed inspection were subjected to post-weld heat treatment at 980 °C for 3 h. The chemical compositions of the weld metal (WM) and base metal (BM), listed in Table 1, conform to ASME specifications.

Microhardness testing was performed using an FM-300 digital microhardness tester equipped with the SVDM3 software system, in accordance with the GB/T 4340.1 standard. Measurements were taken on the capping, filling, and backing passes of the welded joint, as shown in Figure 1(c). Tensile specimens for both room-temperature and high-temperature testing were extracted parallel to the

 doi:10.20944/preprints202512.1597.v1



rolling direction of the Inconel 617 plates, near the weld root. Room-temperature tensile tests were conducted following ASTM A370-23, while high-temperature tests complied with ASTM E21-20 at a test temperature of 750 °C. The geometry of the specimens is shown in Figure 1(d).

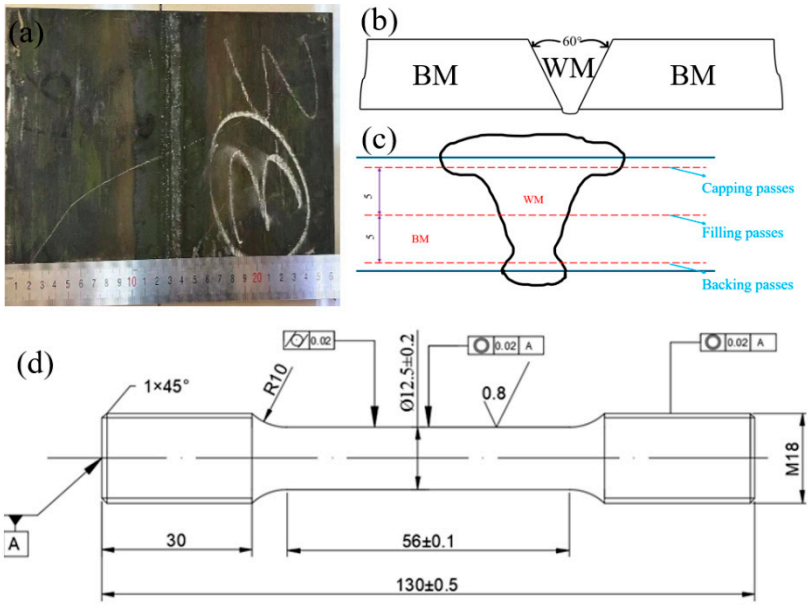


**Figure 1.** (a) Inconel 617 alloy welded joint; (b) Schematic diagram of the welding groove; (c) Schematic diagram of the microhardness testing; (d) Dimensions of the tensile test specimen.

**Table 1.** Chemical composition (wt.%) of BM and WM.

| | C | Si | Cr | Mo | Ti | Al | Co | Fe | Ni |
|---|---|---|---|---|---|---|---|---|---|
| BM | 0.065 | 0.021 | 21.81 | 8.73 | 0.41 | 1.10 | 12.03 | 0.19 | Bal. |
| WM | 0.05 | 0.1 | 21.5 | 9.0 | 0.3 | 1.3 | 11.0 | 0.5 | Bal. |

*2.2. Material Characterization*

The microstructure and precipitates of the Inconel 617 welded joint were characterized using a Leica FEM-4M optical microscope and an FEI Quanta 650 scanning electron microscope (SEM), with energy-dispersive X-ray spectroscopy (EDS) employed for phase identification. The morphology and size of the precipitates were further analyzed using Hitachi H-800 and F20 transmission electron microscopes (TEM). Selected area electron diffraction (SAED) was applied to determine the crystal structures of the precipitates. Samples for optical microscopy (OM) and SEM were ground with progressively finer SiC papers, mechanically polished, and etched in a $CuCl_2$–HCl–ethanol solution (5 g $CuCl_2$ + 100 mL HCl + 100 mL ethanol). TEM foils were prepared by twin-jet electropolishing in a 10% perchloric acid–ethanol solution at −25 °C under a constant current of 80 mA. TEM observations were carried out at an accelerating voltage of 175 kV. After mechanical polishing, the surface of the EBSD specimen is further finished by electrolytic polishing. Electron backscatter diffraction (EBSD) Kikuchi patterns are acquired using a JSM-7200F scanning electron microscope equipped with an Oxford NordlysMax2 detector, and the data are analyzed using Aztec software.

## 3. Results and Discussion

*3.1. Microstructure of the Joint*

The relatively low heat input of the gas tungsten arc welding (GTAW) process helps minimize the heat-affected zone (HAZ), particularly during the welding of Inconel 617 alloy [15]. Owing to its excellent thermal resistance, high-temperature stability, high melting point, and strong oxidation

 doi:10.20944/preprints202512.1597.v1



resistance, Inconel 617 effectively restricts heat diffusion into the base metal during welding. Consequently, the grain structure remains largely unchanged, resulting in a narrow HAZ. In addition, the ERNiCrCoMo-1 filler wire exhibits excellent compatibility with Inconel 617, promoting efficient heat transfer between the weld and base metals and further mitigating thermal effects on the microstructure. The precise control inherent to GTAW—together with its relatively slow travel speed and appropriate cooling measures—effectively suppresses HAZ growth. As a result, the HAZ is extremely limited and often indistinct [16–18]. Therefore, this study primarily focuses on the microstructure and properties of the weld metal, fusion zone, and base metal.

3.1.1. Microstructure and Analysis of the Base Metal

Figure 2 presents the microstructure of the Inconel 617 alloy. The optical micrograph (Figure 2a) shows the base metal composed of equiaxed austenitic grains with an average size of approximately 100 μm. Numerous precipitates are distributed both along grain boundaries and within the grains. Many annealing twins are also observed, indicating continued grain growth during post-weld annealing. The presence of twins at grain-growth fronts suggests atomic stacking events associated with recrystallization [19]. The SEM image of the base metal (Figure 2b) reveals similar features. EDS analyses of precipitates at grain boundaries and within grains (Figures 2c and 2d, respectively) show that the grain-boundary precipitates are Cr-rich, whereas the intragranular precipitates are Ti-rich. According to previous studies [16,17], these correspond to $M_{23}C_6$ and MC carbides, respectively.

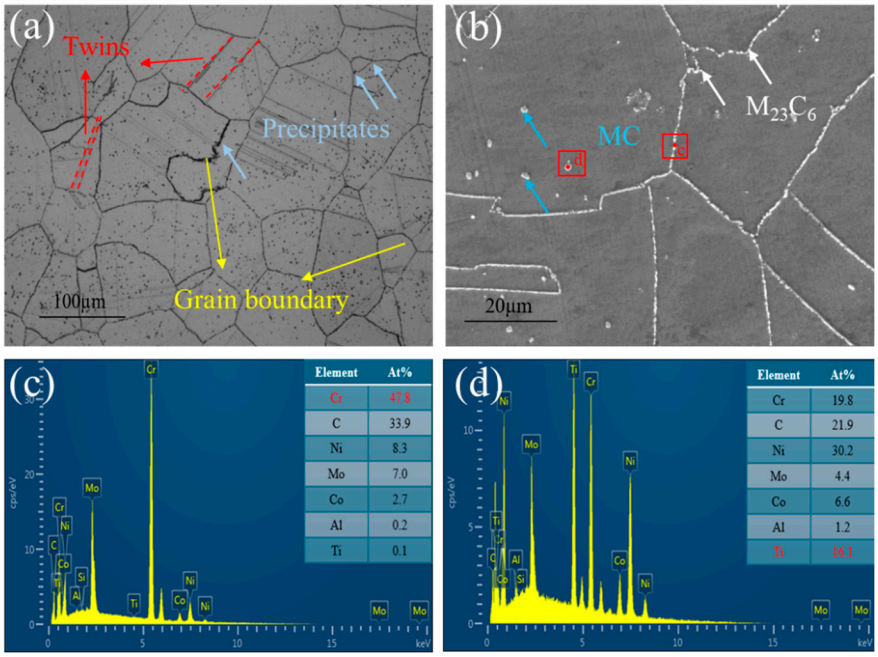


**Figure 2.** (a) Microstructure of the base metal; (b) Ti-rich and Cr-rich phases;(c) EDS of $M_{23}C_6$ precipitates; (d) EDS of MC precipitates.

Figure 3 shows the TEM microstructure of the Inconel 617 alloy substrate. In Figure 3(a), clear interactions between precipitates and dislocations are observed. The intragranular precipitates exert a pronounced pinning effect on dislocation motion, forming a composite strengthening mechanism based on the "dislocation–precipitate" interaction. Distinct dislocation entanglements are also evident, primarily resulting from intense thermal cycling and stress concentration, which lead to significant local strain accumulation [20]. A higher-magnification image of the selected region (Figure 3(b)) further characterizes the precipitates distributed along grain boundaries and within grains. SAED and EDS analyses identify the grain-boundary precipitates as Mo-rich $M_6C$ carbides (Figure 3(c)), while the intragranular, particle-like precipitates correspond to Cr-rich $M_{23}C_6$ carbides (Figure

 doi:10.20944/preprints202512.1597.v1



3(d)). The local accumulation of precipitates may induce stress concentration, serving as potential crack initiation sites, particularly under cyclic or sustained loading. Further fracture analysis is required to confirm this behavior.

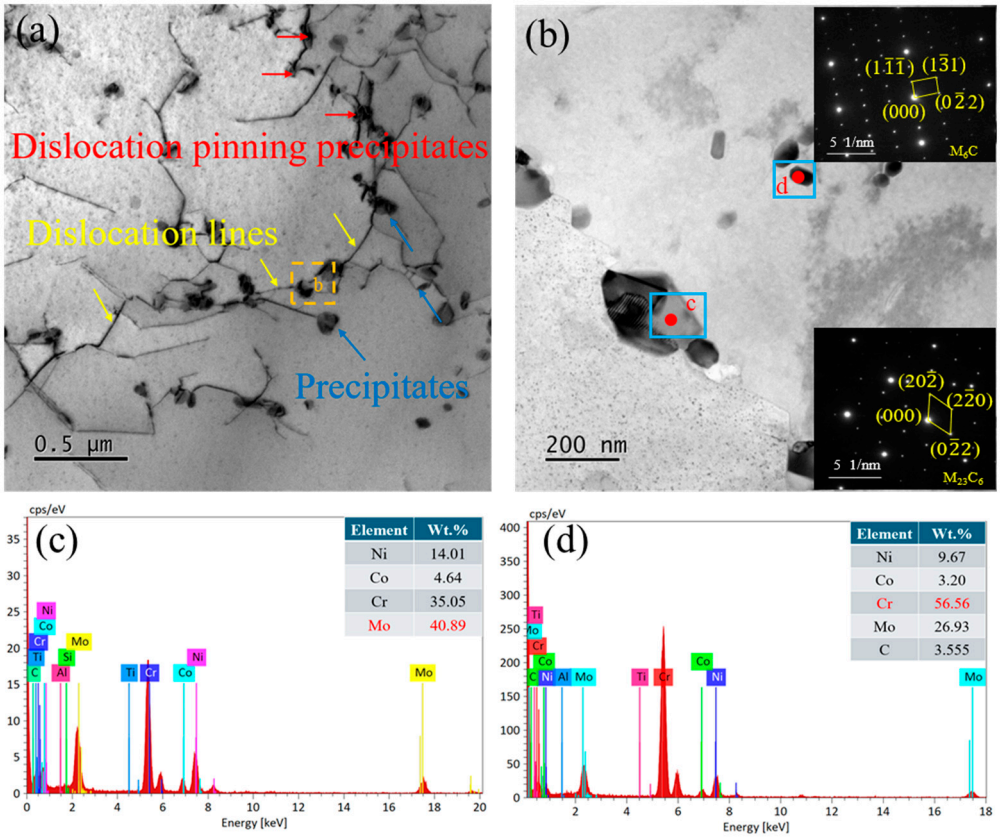


**Figure 3.** (a) TEM image of the base metal; (b) TEM images of $M_6C$ and $M_{23}C_6$ phases in the base metal;(c) EDS of $M_6C$ precipitates (d) EDS of $M_{23}C_6$ precipitates.

### 3.1.2. Microstructure and Analysis of the Fusion Zone

Figure 4(a) shows the SEM image of the fusion zone, where a characteristic bright, strip-like structure is observed along the fusion-line direction. This feature is typical of fusion zones and represents the metallurgical bonding region formed by re-melting and solidification between adjacent melt pools during welding. The bright strip structure appears layered, with distinct interlayer boundaries, indicating that during multi-pass and multi-layer deposition, the melt-pool boundaries were not fully eliminated, leading to slight metallurgical discontinuities. As shown in Figure 4(b), numerous fine particles are distributed along the fusion line, forming chain-like or lattice arrangements along the interface. The region marked by the red box was analyzed by SAED, revealing a crystalline structure with evident twin characteristics and a regular lattice arrangement. Pronounced grain-boundary deflection in this region suggests that thermal effects near the fusion line induced grain growth or partial recrystallization. The particle precipitates act as dislocation-pinning sites, contributing to local strengthening along the fusion line, although they may also serve as potential sources of brittleness [21]. Figure 4(c) presents nanoscale precipitates dispersed within the matrix, exhibiting rod-like or particulate morphologies. SAED analysis confirms that these precipitates correspond to the $M_{23}C_6$ phase, showing specific orientation relationships that indicate preferential growth along certain crystallographic planes during solidification. Owing to repeated thermal cycling, the microstructure in the fusion-line region differs significantly from that of the base matrix. The fine precipitates distributed along the fusion line enhance the local strength through precipitation strengthening and dislocation-pinning mechanisms [22].

 doi:10.20944/preprints202512.1597.v1



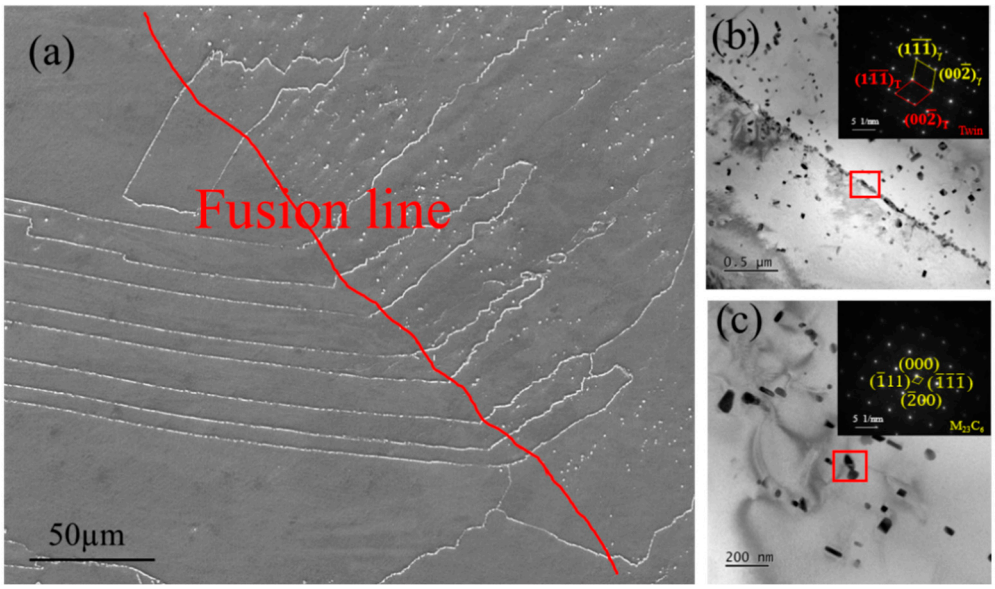


**Figure 4.** (a) SEM image of the weld joint fusion zone; (b) TEM image of the twinned structure at the fusion zone; (c) TEM image of $M_{23}C_6$ at the fusion zone.

3.1.3. Microstructure and Analysis of the Weld Metal

Figure 5 presents the microstructure of the weld region. The SEM image of the weld seam (Figure 5(a)) reveals a dendritic grain structure, with numerous precipitates distributed both along grain boundaries and within grains. SAED and EDS analyses (Figure 5(b)) indicate that the grain-boundary precipitates are Ti-rich MC carbides (Figure 5(d)), surrounded by Cr-rich $M_{23}C_6$ carbides (Figure 5(e)). The TEM image of intragranular regions (Figure 5(c)) shows a high density of fine, particle-like precipitates that impede dislocation motion. The interaction between these precipitates and dislocations is believed to contribute to the increased microhardness observed in the weld metal.

3.1.4. Microstructures at the Interface

No heterogeneous mixing zone or distinct transition layer was observed near the interface. Instead, significant co-crystallization occurred between the weld metal and the base metal, resulting in the formation of a dense solidification grain boundary in the interfacial region. Because both the weld and base metals are compositionally similar Ni-based face-centered cubic (FCC) austenitic high-temperature alloys, effective mutual mixing was achieved under the combined influence of arc forces and surface tension. Consequently, no obvious compositional or microstructural transition zone was detected at the interface. This observation further confirms the excellent compatibility between the weld metal and base metal during welding, consistent with previous studies on interfacial behavior in high-temperature alloy joints [23,24], and supports the interpretation presented in Section 3.1.

As shown in Figure 6, the low heat input of the gas tungsten arc welding (GTAW) process and the steep temperature gradient across the joint promote the formation of numerous columnar dendrites in the weld metal during solidification. These columnar dendrites exhibit pronounced competitive growth behavior, arising from nonuniform heat input during arc heating, which aligns the preferred dendrite growth direction with the maximum temperature gradient. When dendrites with differing orientations intersect, competitive growth occurs. Figure 6(a) shows that the base-metal side of the interface contains cellular crystals of varying sizes, whereas coarse columnar dendrites dominate the fusion zone. Figure 6(b) reveals the presence of numerous low-angle grain boundaries (LAGBs) in the base metal near the interface, primarily attributed to residual stresses generated during cooling. The LAGBs within the columnar dendrites on the weld side originate from elemental segregation during solidification.

 doi:10.20944/preprints202512.1597.v1



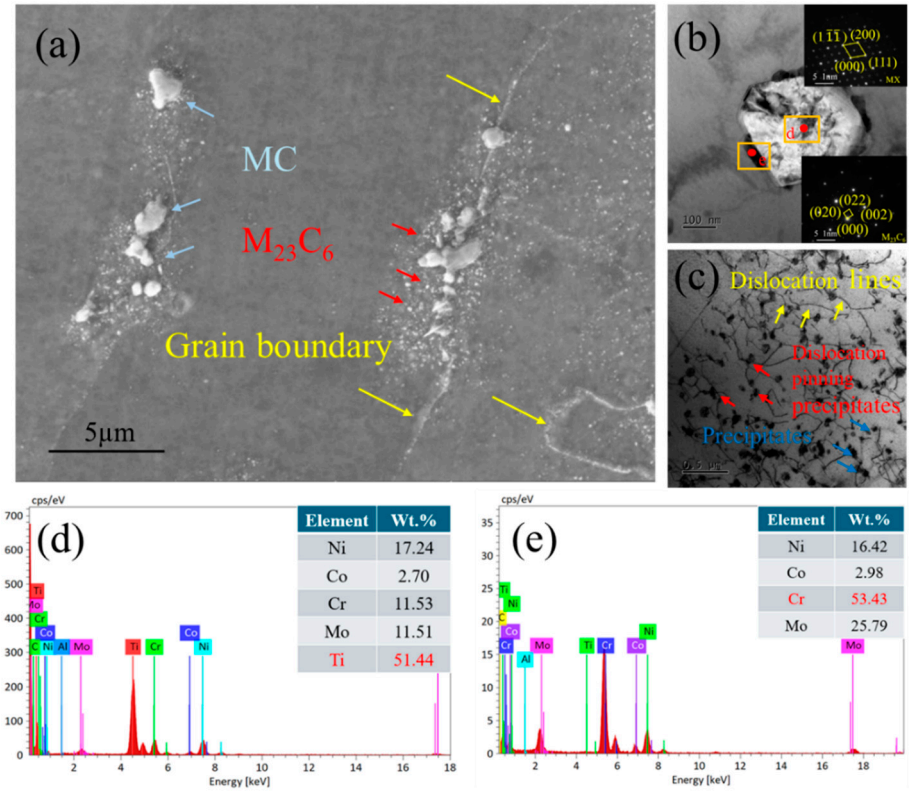


**Figure 5.** (a) SEM image of the weld; (b) TEM image of Ti-rich and Cr-rich phases at the weld; (c) TEM image showing precipitate pinning dislocations at the weld;(d) EDS of MC precipitates; (e) EDS of $M_{23}C_6$ precipitates.

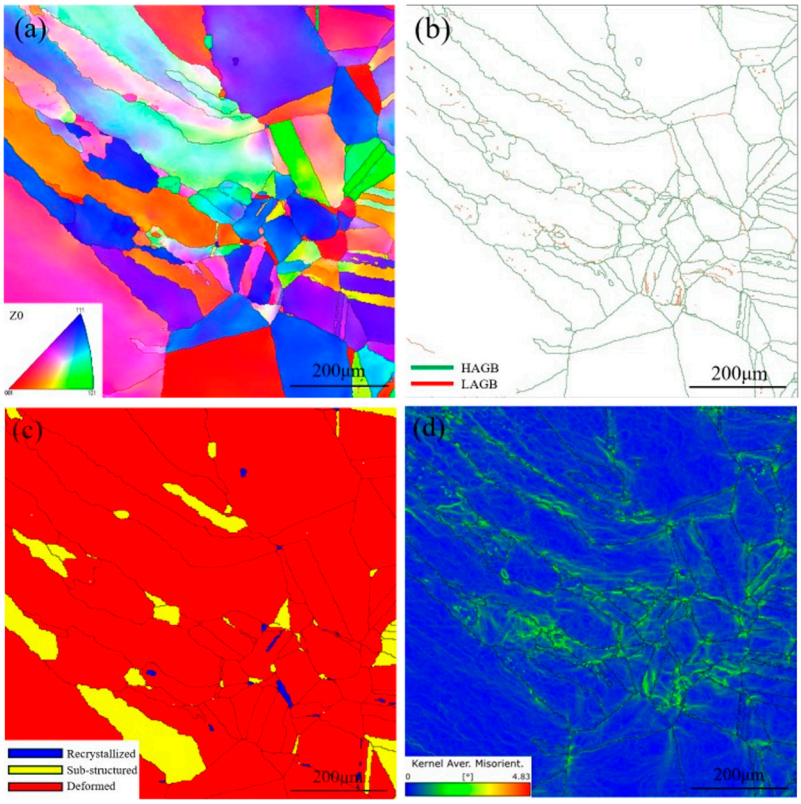


**Figure 6.** EBSD analysis results of the interface: (a) IPF analysis result of the interface; (b) grain boundary character of the interface; (c) grain type distribution of the interface; (d) KAM analysis result of the interface.

 doi:10.20944/preprints202512.1597.v1



Electron backscatter diffraction (EBSD) grain-orientation mapping (Figure 6(c)) indicates that most regions of the welded joint (red) consist of deformed grains characterized by high intragranular misorientation gradients and dislocation densities, suggesting incomplete recrystallization. A smaller fraction of substructured grains (yellow) and recrystallized grains (blue) appear mainly in areas of localized high strain, indicating the onset of dynamic recovery and recrystallization. Kernel average misorientation (KAM) analysis (Figure 6(d)) further reveals localized plastic-strain concentration on the base-metal side of the interface. This behavior arises from differences in the physical properties of the two materials. During weld solidification, the fusion zone near the base-metal side solidifies first. As solidification proceeds, shrinkage-induced stresses develop within the weld metal. When these stresses exceed the local yield strength, plastic deformation occurs at the interface. Because the stress is insufficient to deform the base metal and the weld center remains at elevated temperature, the deformation is primarily confined to the interfacial region.

### *3.2. Mechanical Properties*

#### 3.2.1. Microhardness

Microhardness measurements were performed across different regions of the welded joint, and the results are shown in Figure 7. Within the weld seam, the backing pass exhibited the highest hardness (329 HV), followed by the fill pass (323 HV) and the cap pass (311 HV). As the first welding layer, the backing pass cooled rapidly, resulting in higher hardness. In contrast, the cap pass cooled more slowly and experienced multiple thermal cycles, leading to microstructural tempering and softening, which markedly reduced hardness. Previous studies [25,26] have shown that variations in microhardness are closely associated with grain-refinement mechanisms. Compared with single-pass welding, multi-pass welding promotes grain refinement due to several factors:(a) subsequent thermal cycles induce partial recrystallization and refinement of grains formed in previous passes;(b) the overall heat input gradually decreases as welding progresses, thereby suppressing excessive grain growth; and(c) the preceding passes create a preheating effect that prolongs the $t_{8/5}$ time (the cooling time from 1073 K to 773 K), influencing microstructural evolution. As shown in Figure 7(b), the rapid solidification of the weld seam produces fine columnar or equiaxed grains, resulting in significantly higher hardness compared with the base metal and HAZ—a trend consistent with the Hall–Petch relationship. Furthermore, the dislocation–precipitate interactions discussed in Section 3.1.2 also contribute to the elevated hardness of the weld seam. According to literature reports [27], the transition zone exhibits marked microstructural and property changes caused by welding heat input. Its hardness is generally lower than that of the weld metal but slightly higher than or comparable to the base metal. As shown in Figure 7(c), variations among the different weld passes influence both the extent and hardness response of the transition zone. Local overheating leads to grain coarsening, thereby reducing hardness [28]. The base metal, characterized by its stable microstructure, is unaffected by welding thermal cycles and thus undergoes little grain refinement, as illustrated in Figure 7(d). The precipitation accumulation and stress concentration discussed in Section 3.1.1—which promote crack initiation—reasonably explain the lower microhardness observed in this region.

 doi:10.20944/preprints202512.1597.v1



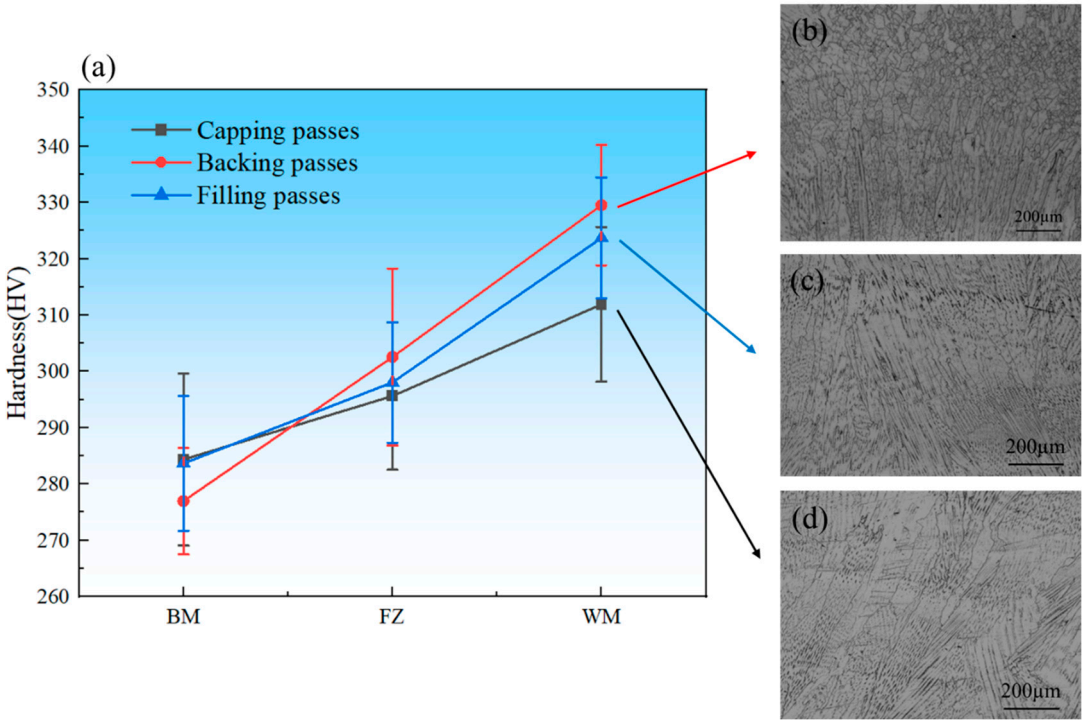


**Figure 7. (a)** Microhardness distribution of the welded joint; **(b)** Metallographic structure of the backing passes; **(c)** Metallographic structure of the filling passes; **(d)** Metallographic structure of the capping passes.

3.2.2. Tensile Properties

Table 2 summarizes the tensile properties of the stabilized welded joints and base metal, including yield strength (YS), ultimate tensile strength (UTS), total elongation (EL), and reduction in area (AR). For clarity, the room-temperature tensile tests for the base metal and welded joint are denoted as BM-RT and Joint-RT, respectively, while the high-temperature tensile tests at 750 °C are referred to as BM-HT-750 and Joint-HT-750. The results show that the tensile strengths of the welded joint at room and high temperatures are 920 MPa and 605.5 MPa, respectively, corresponding to joint efficiencies of 117% and 121%. As illustrated in Figure 8, the fracture locations under both testing conditions are situated within the base metal. This indicates that the strength of the base metal is lower than that of the welded joint, consistent with the trend observed in the microhardness results. The yield and tensile strengths of both the base metal and the welded joint decrease at 750 °C compared with room temperature, primarily due to recovery and softening phenomena, as well as increased damage sensitivity at elevated temperatures [10].

**Table 2.** Tensile results for the Joint and BM.

| Sample No. | Tensile properties | | | |
|---|---|---|---|---|
| | UTS(Mpa) | YS(Mpa) | EL(%) | AR(%) |
| BM-RT | 870 | 392 | 48 | 51 |
| BM-HT-750 | 560 | 301 | 47.5 | 45.5 |
| Joint-RT | 920 | 459 | 37 | 51 |
| Joint-HT-750 | 605.5 | 364 | 30 | 43.5 |

UTS: Ultimate tensile strength, YS: Yield strength, EL: Elongation, AR: Area reduction.

 doi:10.20944/preprints202512.1597.v1



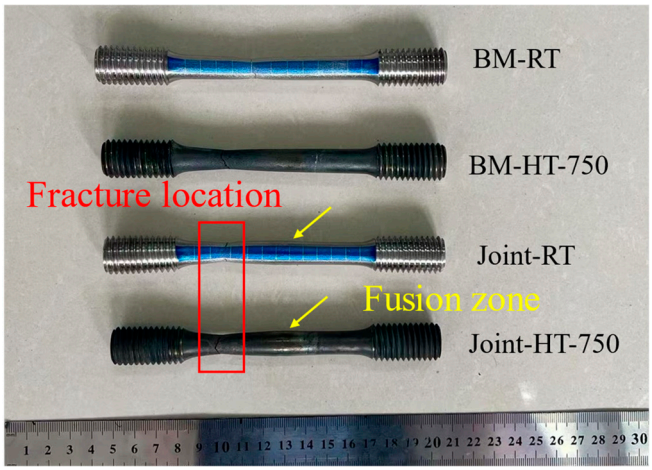


**Figure 8.** Fracture location of the specimens.

*3.3. Fracture Morphology and Deformation Mechanism Analysis of Tensile Specimens*

The fracture morphology of the tensile specimens reveals the fracture modes and characteristic deformation behavior of the welded joint under different conditions. In this study, fractures in both the base metal and welded-joint specimens occurred within the base metal. Because the testing conditions were identical for both specimen types, no significant differences in fracture morphology or fracture mode were observed. Therefore, the following discussion focuses on the macroscopic fracture morphology of the welded-joint tensile specimens.

3.3.1. Fracture Morphology

As shown in Figure 9(a), the macroscopic fracture surface at room temperature exhibits a typical cup-and-cone morphology, consisting of a central fibrous region surrounded by a shear-lip region. At high temperature (Figure 9(d)), the fracture surface displays a similar fibrous–shear-lip configuration but with a noticeably coarser appearance, indicating that fracture occurred through progressive crack propagation rather than an instantaneous event. Compared with the room-temperature specimen, the shear-lip region is significantly reduced, and the fracture surface features more pronounced ductile dimples. Ductile fracture generally manifests as a cup-and-cone surface, arising from localized plastic deformation after the material reaches its ultimate tensile stress. Initially, strain concentrates in a specific region, causing gradual reduction of the cross-sectional area and the formation of necking. With continued deformation, fracture propagates along the cup-and-cone profile, completing the failure process. The central fibrous region contains evident secondary cracks, while a relatively narrow shear-lip region surrounds it. As shown in Figure 9(b), the fibrous region exhibits ductile intergranular fracture with secondary cracks distributed along grain boundaries. Irregular depressions and tearing ridges indicate substantial plastic flow and localized deformation during fracture, consistent with ductile behavior. In Figure 9(c), numerous closely spaced dimples characteristic of the microvoid-coalescence mechanism are observed, suggesting that microvoids nucleated, grew, and eventually coalesced during tensile loading, leading to final rupture. At high temperature (Figure 9(f)), the dimples are predominantly spherical, deep, and densely packed, implying that the material absorbed considerable plastic deformation energy prior to fracture. The tensile load direction is approximately perpendicular to the fracture surface, further confirming the ductile-tensile fracture mode. Moreover, the absence of cleavage facets and river-pattern striations rules out the possibility of a cleavage-type fracture.

 doi:10.20944/preprints202512.1597.v1



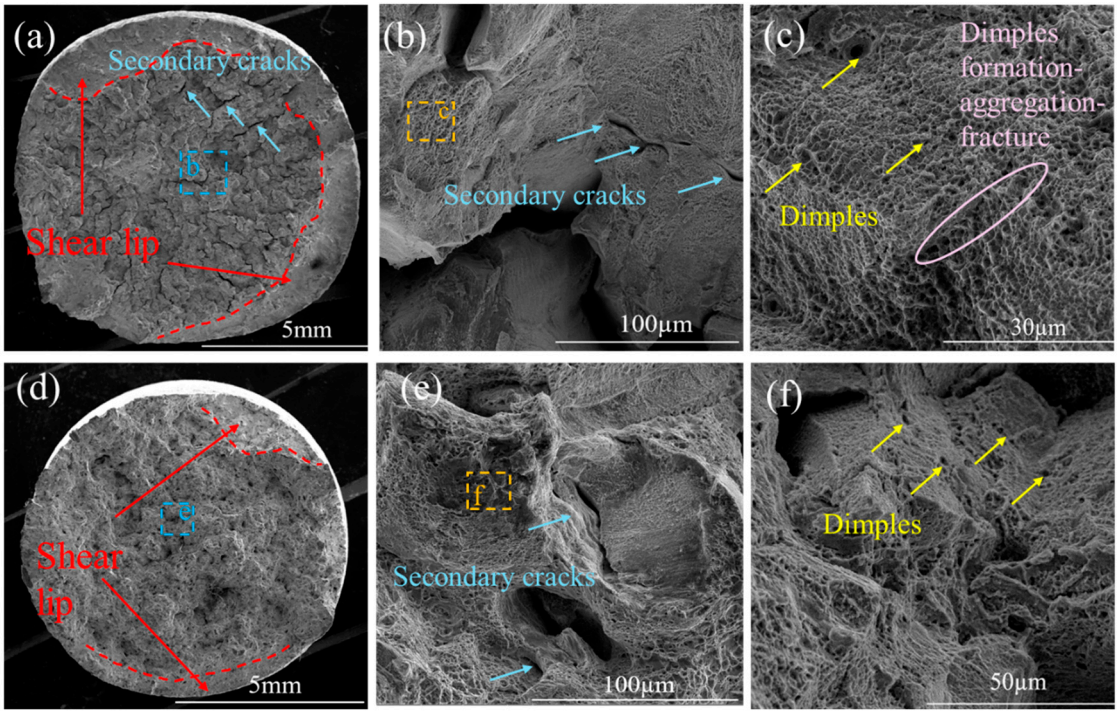


**Figure 9.** (a-c) Fracture surface micrographs of Joint-RT after tensile testing; (d-f) Fracture surface micrographs of Joint-HT-750 after tensile testing.

3.3.2. Deformation Microstructure and Precipitation Analysis of the Joint

The deformation microstructure developed during tensile testing is critical for elucidating the fracture mechanism. Therefore, the post-deformation microstructures of the specimens were thoroughly characterized. As shown in Figure 10(a), after room-temperature deformation, the microstructure is dominated by parallel dislocation slip bands (DSBs), with a small number of deformation twins identified by SAED (Figure 10(b)). After high-temperature deformation, a limited number of parallel DSBs remain visible (Figure 10(c)). In addition, pronounced dislocation entanglement is observed between slip bands, accompanied by numerous deformation twins (Figure 10(d)).

For face-centered cubic (FCC) alloys such as Inconel 617, low stacking-fault energy (SFE) promotes deformation twinning. When dislocation motion is hindered by dislocation accumulation or by unfavorable slip orientations, twinning is activated as a supplementary mechanism to accommodate plastic strain. Twin boundaries, as planar defects analogous to high-angle grain boundaries, can effectively impede dislocation motion. Dislocations near these twin boundaries experience significant constraint, resulting in dislocation pile-ups and elevated local dislocation density, as shown in the magnified region of Figure 10 [29].

At room temperature, the dominant deformation mechanism is dislocation slip, with limited twinning activity. Because Inconel 617 possesses relatively high SFE at room temperature, dislocation glide is favored over twinning. Twinning requires higher shear stress, and it occurs locally when slip is obstructed and local stress concentrations develop. By contrast, at high temperature (Figure 10(c)), deformation twinning becomes the primary deformation mode, accompanied by minor slip activity. The SFE of Inconel 617 decreases with increasing temperature, leading to dislocation dissociation into partials that readily form twins [30,31]. Under such conditions, dislocations can also climb more easily, preventing their accumulation and the formation of pronounced slip bands. Furthermore, during high-temperature deformation, dynamic recovery and even dynamic recrystallization may occur, reducing the dislocation density and suppressing the observable development of slip bands.

 doi:10.20944/preprints202512.1597.v1



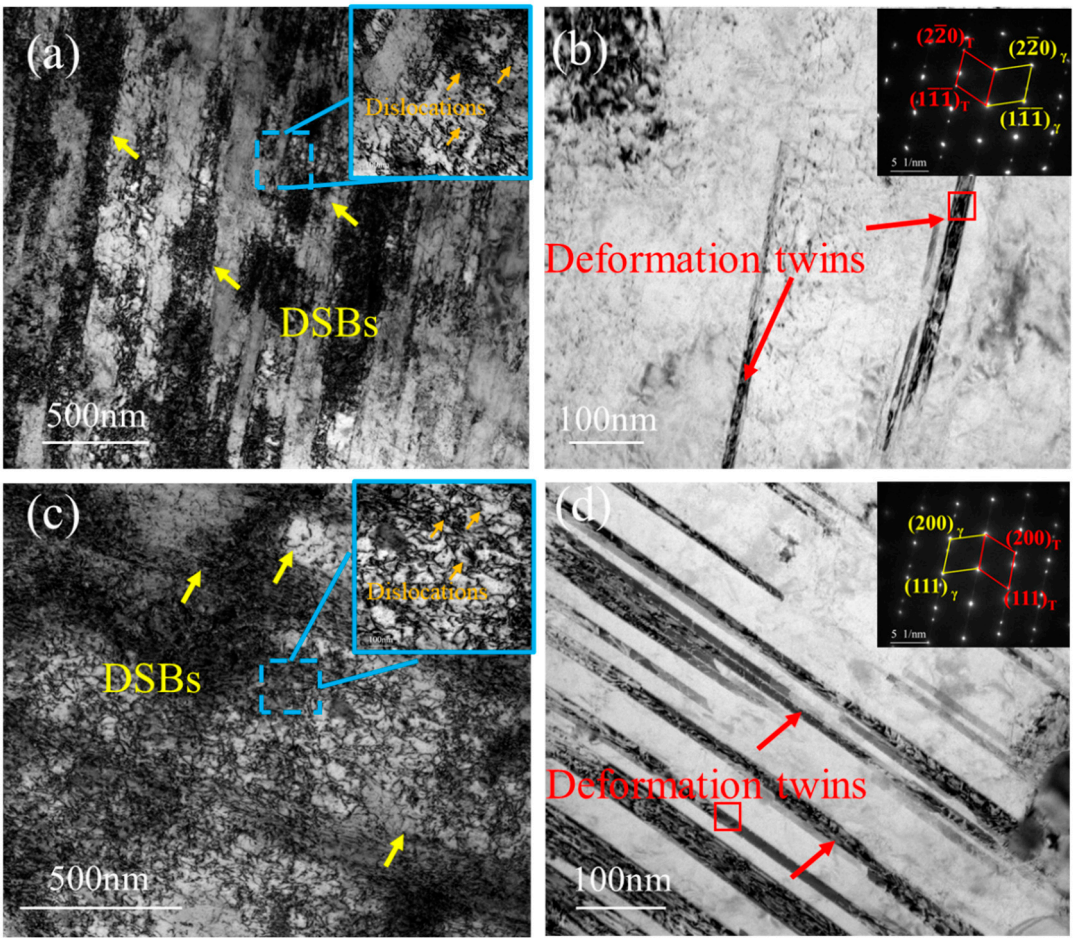


**Figure 10.** (a) TEM image of slip bands and dislocations during tensile deformation of Joint-RT; (b) TEM image of deformation twins in Joint-RT; (c) TEM image of slip bands and dislocations during tensile deformation of Joint-HT-750; (d) TEM image of deformation twins in Joint-HT-750.

To further investigate the evolution of precipitates under tensile deformation, TEM was employed, complemented by EDS for compositional characterization. Figure 11(a) shows the precipitates in the joint after room-temperature deformation, where intergranular carbides are identified by EDS as Cr-rich $M_{23}C_6$ (Figure 11(c)). After high-temperature deformation (Figure 11(b)), precipitates are observed along twin boundaries and are likewise confirmed by EDS to be Cr-rich $M_{23}C_6$ (Figure 11(d)). These results indicate that $M_{23}C_6$ remains the dominant precipitate phase after tensile deformation. No Mo-rich $M_6C$ or Ti-rich MC carbides were detected in the TEM analysis. This predominance of $M_{23}C_6$ is consistent with previous reports on Inconel 617 [32–34].

Studies of long-term high-temperature exposure (649–1093 °C) have shown that $M_{23}C_6$ is the principal stable phase in Inconel 617, with negligible formation of MC or $M_6C$ [35,36]. Within the 600–950 °C range, Mo atoms exhibit a solubility limit of approximately 10–15%, whereas Cr atoms show a significantly higher limit of 32–43%. Because of the much lower solubility of Mo, pre-existing carbides are unlikely to dissolve into the matrix and reprecipitate as new carbides. Moreover, at elevated temperatures, the $M_{23}C_6$ precipitates located between twin boundaries serve as obstacles to dislocation glide, altering dislocation trajectories and restricting slip. This obstruction likely promotes deformation twinning within the grains under high-temperature conditions.

 doi:10.20944/preprints202512.1597.v1



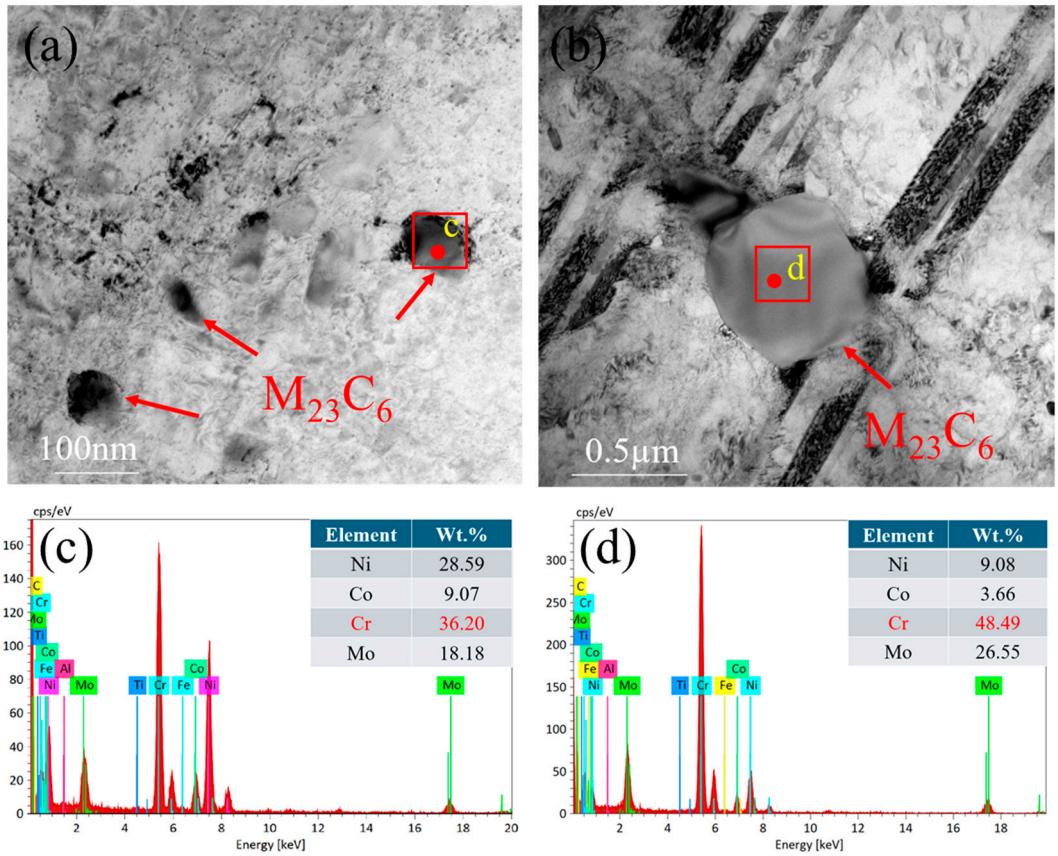


**Figure 11.** (a) TEM image of Cr-rich precipitates during tensile deformation of Joint-RT; (b) TEM image of Cr-rich precipitates during tensile deformation of Joint-HT-750. (c) EDS of $M_{23}C_6$ precipitates; (d) EDS of $M_{23}C_6$ precipitates.

3.3.3. Overview of the Deformation Mechanisms in the Tensile Behavior of the Joint

In summary, the deformation mechanisms of the Inconel 617 welded joint after tensile testing at room and elevated temperatures are illustrated in Figure 12. At room temperature, deformation is dominated by planar slip and dislocation entanglement. As shown in Figure 12(a), numerous parallel slip bands develop within the grains, accompanied by pronounced dislocation tangling between these bands. With increasing strain, dislocation motion becomes progressively constrained, leading to the formation of deformation twins. These twins facilitate plastic deformation by redistributing local stresses and alleviating stress concentrations. Moreover, interactions between $M_{23}C_6$ precipitates and the matrix act as obstacles to dislocation glide, increasing the resistance to plastic flow and influencing the overall tensile response.

At elevated temperatures, the deformation behavior changes markedly, as depicted in Figure 12(b). The reduced stacking-fault energy promotes deformation twinning, while the higher mobility of dislocations leads to fewer slip bands. Consequently, deformation twinning becomes the dominant mechanism under high-temperature conditions, accompanied by limited slip activity. Overall, plastic deformation at room temperature is primarily governed by dislocation slip and entanglement, with minor twinning, whereas at elevated temperature, deformation twinning predominates. Additionally, $M_{23}C_6$ precipitates serve as pinning sites for dislocations, further modifying their motion paths and contributing to the observed deformation behavior.

 doi:10.20944/preprints202512.1597.v1



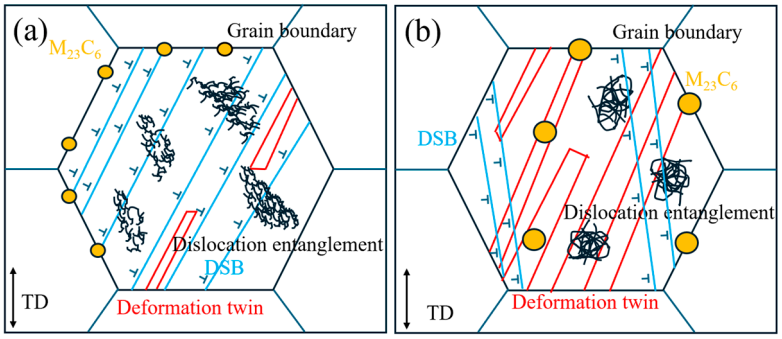


**Figure 12.** Schematic of the tensile deformation mechanisms in Inconel 617 welded joints.

## 4. Conclusions

The microstructure of the Inconel 617 alloy and ERNiCrCoMo-1 filler wire GTAW welded joint was studied. The microhardness and uniaxial tensile properties of the joint at room temperature and 750 °C were systematically tested, and the tensile fracture was analyzed. Based on the research findings, the following conclusions can be drawn:

(1) The primary precipitates in the base metal are Cr-rich $M_{23}C_6$ and Ti-rich MC. In the welded joint, precipitates are mainly concentrated in the fusion zone and weld metal, predominantly comprising $M_{23}C_6$ and MC. The fusion-line region experiences multiple thermal cycles, leading to grain growth and partial recrystallization. These precipitates serve as pinning sites for dislocations, thereby enhancing strength but concurrently reducing plasticity.

(2) The weld metal and base metal exhibit excellent compositional compatibility and co-crystallization at the interface, with no discernible microstructural or compositional transition zone. Plastic deformation near the interface is mainly concentrated on the base-metal side, indicating strong metallurgical bonding and structural stability of the interface during welding.

(3) The welded joints exhibit excellent mechanical integrity, achieving tensile strengths of 920 MPa at room temperature and 605.5 MPa at 750 °C, corresponding to joint efficiencies of 117% and 121%, respectively. All fractures occur within the base metal, confirming the high quality and reliability of the welds.

(4) The hardness of the welded joint varies significantly across different welding passes, with the highest value of 329 HV observed in the backing pass and the lowest of 311 HV in the cap pass. The weld metal exhibits higher hardness than the base metal, primarily due to grain refinement and precipitation strengthening during welding. The elevated hardness and strength of the weld region are attributed to grain refinement, precipitation hardening, and dislocation–precipitate interactions, consistent with the Hall–Petch relationship. The dense distribution of $M_{23}C_6$ precipitates and the fine dendritic substructure collectively contribute to local strengthening.

(5) Deformation behavior is strongly temperature-dependent. At room temperature, plasticity is governed by planar slip and dislocation entanglement, with limited twinning. At elevated temperatures, deformation twinning becomes the dominant mechanism due to the reduced stacking-fault energy and the pinning effect of $M_{23}C_6$ carbides on dislocation motion. These mechanisms collectively account for the excellent high-temperature strength and ductility of the GTAW-welded Inconel 617 joints.

## References

1. Chen Y, Xu M, Zhang T, et al. Grain refinement and mechanical properties improvement of Inconel 625 alloy fabricated by ultrasonic-assisted wire and arc additive manufacturing. *J Alloys Compd.* **2022**, *910*, 164957, https://doi.org/10.1016/j.jallcom.2022.164957

2. Tsigkis V, Rahman M S, Hackel L, et al. Helium tribology of Inconel 617 subjected to laser peening for high temperature nuclear reactor applications. *Appl Surf Sci.* **2022**, *577*, 151961, https://doi.org/10.1016/j.apsusc.2021.151961
3. Sah I, Park J, Kim E S. Fatigue life curves of alloy 617 in the temperature range of 800–950° C. *Nucl Eng Technol*. **2023**, *55*, 546-554. https://doi.org/10.1016/j.net.2022.09.027
4. Chen M S, Wang G Q, Li H B, et al. Annealing treatment methods and mechanisms for refining mixed and coarse grains in a solution treatment nickel-based superalloy. *Adv Eng Mater*. **2019**, *21*, 1900558. https://doi.org/10.1002/adem.201900558
5. He D G, Lin Y C, Tang Y, et al. Influences of solution cooling on microstructures, mechanical properties and hot corrosion resistance of a nickel-based superalloy. *Mater Sci Eng A*. **2019**, *746*, 372-383. https://doi.org/10.1016/j.msea.2019.01.015
6. Adamiec J, Konieczna N. Assessment of the hot cracking susceptibility of the Inconel 617 nickel-based alloy. *Arch Metall Mater*. **2021**, *66*, 10.24425/amm.2021.134781
7. Zhang Y, Jing H, Xu L, et al. Design and performance of weld filler metal to match an advanced heat-resistant Fe-Cr-Ni alloy. *Mater Sci Eng A*. **2018**, *721*, 103-116. https://doi.org/10.1016/j.msea.2018.02.037
8. Zhao L, Jing H, Xu L, et al. Investigation on mechanism of type IV cracking in P92 steel at 650° C. *J Mater Res*. **2011**, *26*, 934-943. https://doi.org/10.1557/jmr.2011.11
9. Zhao L, Jing H, Xu L, et al. Experimental study on creep damage evolution process of Type IV cracking in 9Cr–0.5 Mo–1.8 W–VNb steel welded joint. *Eng Fail Anal*. **2012**, *19*, 22-31. https://doi.org/10.1016/j.engfailanal.2011.09.003
10. Zhang Y, Jing H, Xu L, et al. Microstructure and mechanical performance of welded joint between a novel heat-resistant steel and Inconel 617 weld metal. *Mater Charact*. **2018**, *139*, 279-292. https://doi.org/10.1016/j.matchar.2018.03.012
11. Kumar A, Pandey C. The Behavior of Dissimilar Welded Joint of Alloy 617/P92 Steel at High Temperatures. *J Mater Eng Perform*. **2025**, 1-9, https://doi.org/10.1007/s11665-025-10652-5
12. Kumar A, Pandey C. Creep rupture and microstructural analysis of dissimilar welded joints of P92 steel and Alloy 617. *Weld Int*. **2025**, *39*, 23-31. https://doi.org/10.1080/09507116.2024.2442480
13. Kumar R, Sirohi S. Microstructure and Mechanical Behavior Study of the GTAW Joint of AISI 310 and Modified 9Cr-1Mo (P91) Steel. *J Mater Eng Perform*. **2025**, 1-19, https://doi.org/10.1007/s11665-025-10820-7
14. Dak G, Guguloth K, Bhattacharyya A, et al. Failure study of creep and high-temperature tensile tested tungsten inert gas welded P92 steel and AISI 304L steel dissimilar weld joints. *J Mater Eng Perform*. **2025**, *34*, 658-685, https://doi.org/10.1007/s11665-023-09070-2
15. Kumar A, Singhal A, Sirohi S, et al. Pulsed current GTAW Inconel 625/AISI 304 L steel dissimilar joint: Microstructure and mechanical properties. *J Constr Steel Res*. **2025**, *231*, 109602, https://doi.org/10.1016/j.jcsr.2025.109602
16. Hao J, Wang C, Duan H, et al. Prediction model for austenite grain size in CGHAZ of TiN-containing steel: considering minimum pinning force and austenite coarsening dynamics. *J Iron Steel Res Int*. **2025**, 1-15, https://doi.org/10.1007/s42243-025-01505-5
17. Shi X, Liu Y, Zhang M, et al. Dual-constricted plasma arc cladding of Inconel 625 alloy: arc characteristics, microstructure, and corrosion resistance. *J Mater Sci: Mater Eng*. **2025**, *20*, 43, https://doi.org/10.1186/s40712-025-00262-3
18. Amirian B, Asad A, Krezan L, et al. A new perspective on the mechanical behavior of Inconel 617 at elevated temperatures for small modular reactors. *Scr Mater*. **2025**, *261*, 116605, https://doi.org/10.1016/j.scriptamat.2025.116605
19. Kumar A, Pandey C. Some studies on dissimilar welds joint P92 steel and Inconel 617 alloy for AUSC power plant application. *Int J Press Vessels Pip*. **2022**, *198*, 104678, https://doi.org/10.1016/j.ijpvp.2022.104678
20. Kumar A, Pandey S M, Sirohi S, et al. P92 steel and inconel 617 alloy welds joint produced using ERNiCr-3 filler with GTAW process: solidification mechanism, microstructure, mechanical properties and residual stresses. *Pandey Arch Civ Mech Eng*. **2023**, *9*, 10.1016/j.heliyon.2023.e18959

 doi:10.20944/preprints202512.1597.v1




21. Kumar G P, Balasubramanian K R. Experimental investigation on high-temperature tensile behavior of cold metal transfer pulse multi-control welding of Inconel 617 alloy. *Results Surf Interfaces.* **2023**, *10*, 100100, https://doi.org/10.1016/j.rsurfi.2023.100100
22. Rathore S, Kumar A, Sirohi S, et al. Role of buttering layer composition on microstructural heterogeneity and mechanical properties of Alloy 617 and P92 steel dissimilar welded joints for future Indian AUSC program. *Int J Adv Manuf Technol.* **2024**, *133*, 671-700, https://doi.org/10.1007/s00170-024-13747-w
23. Cui Y, Xu CL, Han Q. Effect of ultrasonic vibration on unmixed zone formation. *Scripta Mater.* **2006**, *55*, 975–8, https://doi.org/10.1016/j.scriptamat.2006.08.035
24. Soysal T, Kou S, Tat D, Pasang T. Macrosegregation in dissimilar-metal fusion welding. *Acta Mater.* **2016**, *110*, 149–60, https://doi.org/10.1016/j.actamat.2016.03.004
25. Jian H G, Wang Y, Tang X M, et al. Microstructure characteristics in multi-pass welding interface of Al-Mg alloy. *Applied Mechanics and Materials.* **2014**, *584*, 921-924. https://doi.org/10.4028/www.scientific.net/AMM.584-586.921
26. Ghumman K Z, Ali S, Din E U, et al. Experimental investigation of effect of welding parameters on surface roughness, micro-hardness and tensile strength of AISI 316L stainless steel welded joints using 308L filler material by TIG welding. *J Mater Res Technol.* **2022**, *1*, 220-236, https://doi.org/10.1016/j.jmrt.2022.09.016
27. Song J, Chen Y, Hao X, et al. Microstructure and mechanical properties of novel Ni–Cr–Co-based superalloy GTAW joints. *J Mater Res Technol.* **2024**, *29*, 2758-2767, https://doi.org/10.1016/j.jmrt.2024.01.241
28. Singh A N, Moitra A, Bhaskar P, et al. Effect of thermal aging on microstructure, hardness, tensile and impact properties of Alloy 617. *Mater Sci Eng A.* **2018**, *710*, 47-56, https://doi.org/10.1016/j.msea.2017.10.078
29. Remy L. The interaction between slip and twinning systems and the influence of twinning on the mechanical behavior of fcc metals and alloys. *Metall Trans A.* **1981**, *12*, 387-408, https://doi.org/10.1007/BF02648536
30. Zhang Y, Tao N R, Lu K. Effects of stacking fault energy, strain rate and temperature on microstructure and strength of nanostructured Cu–Al alloys subjected to plastic deformation. *Acta Mater.* **2011**, *59*, 6048-6058, https://doi.org/10.1016/j.actamat.2011.06.013
31. Meyers M A, Vöhringer O, Lubarda V A. The onset of twinning in metals: a constitutive description. *Acta Mater.* **2001**, *49*, 4025-4039, https://doi.org/10.1016/S1359-6454(01)00300-7
32. Kaoumi D, Hrutkay K. Tensile deformation behavior and microstructure evolution of Ni-based superalloy 617. *J Nucl Mater.* **2014**, *454*, 265-273, https://doi.org/10.1016/j.jnucmat.2014.08.003
33. Chomette S, Gentzbittel J M, Viguier B. Creep behaviour of as received, aged and cold worked INCONEL 617 at 850 °C and 950 °C. *J Nucl Mater.* **2010**, *399*, 266-274, https://doi.org/10.1016/j.jnucmat.2010.01.019
34. Kihara S, Newkirk J B, Ohtomo A, et al. Morphological changes of carbides during creep and their effects on the creep properties of Inconel 617 at 1000 °C. *Metall Trans A.* **1980**, *11*, 1019-1031, https://doi.org/10.1007/BF02654716
35. Roy A K, Marthandam V. Mechanism of yield strength anomaly of Alloy 617. *Mater Sci Eng A.* **2009**, *517*, 276-280, https://doi.org/10.1016/j.msea.2009.03.090
36. Kourtoukova G L, Demetry C, Ramanath S, et al. Design and tailoring of Ni–Sn–W composites for bonded abrasive applications. *Mater Sci Eng A.* **2000**, *276*, 58-69, https://doi.org/10.1016/S0921-5093(99)00516-X